



HAL
open science

Electrical properties of cometary dust particles derived from line shapes of TOF-SIMS spectra measured by the ROSETTA/COSIMA instrument

Klaus Hornung, Eva Maria Mellado, John Paquette, Nicolas Fray, Henning Fischer, Oliver Stenzel, Donia Baklouti, Sihane Merouane, Yves Langevin, Anais Bardyn, et al.

► To cite this version:

Klaus Hornung, Eva Maria Mellado, John Paquette, Nicolas Fray, Henning Fischer, et al.. Electrical properties of cometary dust particles derived from line shapes of TOF-SIMS spectra measured by the ROSETTA/COSIMA instrument. *Planetary and Space Science*, 2020, 182, pp.104758. <10.1016/j.pss.2019.104758>. <insu-02309198>

HAL Id: insu-02309198

<https://insu.hal.science/insu-02309198v1>

Submitted on 9 Oct 2019

HAL is a multi-disciplinary open access archive for the deposit and dissemination of scientific research documents, whether they are published or not. The documents may come from teaching and research institutions in France or abroad, or from public or private research centers.

L'archive ouverte pluridisciplinaire HAL, est destinée au dépôt et à la diffusion de documents scientifiques de niveau recherche, publiés ou non, émanant des établissements d'enseignement et de recherche français ou étrangers, des laboratoires publics ou privés.



HAL Authorization

Journal Pre-proof



Electrical properties of cometary dust particles derived from line shapes of TOF-SIMS spectra measured by the ROSETTA/COSIMA instrument

Klaus Hornung, Eva Maria Mellado, John Paquette, Nicolas Fray, Henning Fischer, Oliver Stenzel, Donia Baklouti, Sihane Merouane, Yves Langevin, Anais Bardyn, Cecile Engrand, Hervé Cottin, Laurent Thirkell, Christelle Briois, Paola Modica, Jouni Rynö, Johan Silen, Rita Schulz, Sandra Siljeström, Harry Lehto, Kurt Varmuza, Andreas Koch, Jochen Kissel, Martin Hilchenbach

PII: S0032-0633(19)30152-7

DOI: <https://doi.org/10.1016/j.pss.2019.104758>

Reference: PSS 104758

To appear in: *Planetary and Space Science*

Received Date: 17 April 2019

Accepted Date: 24 September 2019

Please cite this article as: Hornung, K., Mellado, E.M., Paquette, J., Fray, N., Fischer, H., Stenzel, O., Baklouti, D., Merouane, S., Langevin, Y., Bardyn, A., Engrand, C., Cottin, Hervé., Thirkell, L., Briois, C., Modica, P., Rynö, J., Silen, J., Schulz, R., Siljeström, S., Lehto, H., Varmuza, K., Koch, A., Kissel, J., Hilchenbach, M., Electrical properties of cometary dust particles derived from line shapes of TOF-SIMS spectra measured by the ROSETTA/COSIMA instrument, *Planetary and Space Science* (2019), doi: <https://doi.org/10.1016/j.pss.2019.104758>.

This is a PDF file of an article that has undergone enhancements after acceptance, such as the addition of a cover page and metadata, and formatting for readability, but it is not yet the definitive version of record. This version will undergo additional copyediting, typesetting and review before it is published in its final form, but we are providing this version to give early visibility of the article. Please note that, during the production process, errors may be discovered which could affect the content, and all legal disclaimers that apply to the journal pertain.

© 2019 Published by Elsevier Ltd.

1 Electrical properties of cometary dust particles derived from line shapes of TOF-SIMS spectra
2 measured by the ROSETTA/COSIMA instrument.

3

4 Klaus Hornung^{1,a}, Eva Maria Mellado¹, John Paquette², Nicolas Fray³, Henning Fischer², Oliver
5 Stenzel², Donia Baklouti⁴, Sihane Merouane², Yves Langevin⁴, Anais Bardyn⁵, Cecile Engrand⁶,
6 Hervé Cottin³, Laurent Thirkell⁷, Christelle Briois⁷, Paola Modica⁷, Jouni Rynö⁸, Johan Silen⁸,
7 Rita Schulz⁹, Sandra Siljeström¹⁰, Harry Lehto¹¹, Kurt Varmuza¹², Andreas Koch¹³, Jochen
8 Kassel², Martin Hilchenbach².

9

10 (1) Universität der Bundeswehr München, LRT-7, 85577 Neubiberg, Germany.

11 (2) Max-Planck-Institut für Sonnensystemforschung, Justus von Liebig Weg 3, 37077 Göttingen,
12 Germany.

13 (3) Laboratoire Interuniversitaire des Systèmes Atmosphériques (LISA), UMR CNRS 7583,
14 Université Paris-Est-Créteil, Université de Paris, Institut Pierre Simon Laplace (IPSL), Créteil,
15 France.

16 (4) Institut d'Astrophysique Spatiale, CNRS / Université Paris Sud, Bâtiment 121, 91405 Orsay,
17 France.

18 (5) DTM, Carnegie Institution of Washington, Washington, DC, USA.

19 (6) Centre de Sciences Nucléaires et de Sciences de la Matière, Bat.104, 91405 Orsay
20 Campus, France.

21 (7) Laboratoire de Physique et Chimie de l'Environnement et de l'Espace(LPC2E), UMR CNRS
22 7328, Université d'Orléans, F-45071 Orléans, France.

23 (8) Finnish Meteorological Institute, Climate Research, Erik Palmenin aukio 1, P.O.Box 503, FI-
24 00101 Helsinki, Finland.

25 (9) European Space Agency, Scientific Support Office, Keplerlaan 1, Postbus 299, 2200 AG
26 Noordwijk, The Netherlands.

27 (10) RISE Research Institutes of Sweden, Bioscience and Materials, Chemistry, Materials and
28 Surfaces, Box 5607, SE-114 86 Stockholm, Sweden.

29 (11) Tuorla Observatory, Department of Physics and Astronomy, University of Turku,
30 Väisäläntie 20, 33 21500 Piikkiö, Finland.

31 (12) Institute of Statistics and Mathematical Methods in Economics, Vienna University of
32 Technology, Wiedner Hauptstrasse 7/105-6, 1040 Vienna, Austria.

33 (13) Von Hoerner und Sulger GmbH, Schlossplatz 8, 68723 Schwetzingen, Germany.

34

35

36 Keywords: Cometary dust, Rosetta mission, electrical properties, time-of-flight mass spectra,
37 sample charging.

38 ^{a)} klaus.hornung@unibw.de.

39

40

41

42

43

44

45 Abstract:

46 Between Aug. 2014 and Sept. 2016, while ESA's cornerstone mission Rosetta was operating in
47 the vicinity of the nucleus and in the coma of comet 67P/Churyumov-Gerasimenko, the
48 COSIMA instrument collected a large number of dust particles with diameters up to a millimeter.
49 Positive or negative ions were detected by a time-of-flight secondary ion mass spectrometer
50 (TOF-SIMS) and the composition of selected particles was deduced. Many of the negative ion
51 mass spectra show, besides mass peaks at the correct position, an additional, extended
52 contribution at the lower mass side caused by partial charging of the dust. This effect, usually
53 avoided in SIMS applications, can in our case be used to obtain information on the electrical
54 properties of the collected cometary dust particles, such as the specific resistivity ($\rho_r > 1.2 \cdot$
55 $10^{10} \Omega m$) and the real part of the relative electrical permittivity ($\epsilon_r < 1.2$). From these values a
56 lower limit for the porosity is derived ($P > 0.8$).

57

58 1. Introduction

59 The COSIMA instrument (COmetary Secondary Ion Mass Analyser, Kissel et al. 2007) collected
60 dust particles in the inner coma of comet 67P in an unprecedented state of preservation due to
61 the impact at low speeds (a few m/s) onto highly porous and low reflectance metal targets
62 (Schulz et al. 2015, Hilchenbach et al. 2016). During the 2 years of the comet escort phase, the
63 instrument continuously measured and transmitted mass spectra from the collected dust
64 particles, contributing to numerous aspects of their chemical composition. The elemental
65 composition of the 67P particles is similar, within a factor of 3, to the one of CI chondrites for the
66 inorganic fraction. As already measured in the particles of 1P/Halley, the 67P particles have a
67 large enrichment in carbon compared to CI chondrites and the organic matter could represent
68 about 45% of the mass of the cometary particles (Bardyn et al., 2017). The carbonaceous
69 matter should be of high molecular weight (Fray et al., 2016) with a N/C = 0.035 ± 0.011 (Fray

70 et al. 2017) and $H/C = 1.04 \pm 0.16$ (Isnard et al., 2019, in press). The cometary H/C elemental
71 ratios are in most cases higher than the values found in the Insoluble Organic Matter (IOMs),
72 extracted from carbonaceous chondrites. This could imply that cometary organic matter is less
73 altered than the organic matter in chondritic IOMs. Evidence for calcium-aluminium-rich
74 inclusions (CAI's) has been found in one of the dust particles (Paquette 2016). The isotopic
75 ratios $^{34}S/^{32}S$ and $^{18}O/^{16}O$ are both consistent with the terrestrial standards within the error bars,
76 but the sulfur ratio is significantly higher than that measured in several gaseous species in the
77 coma of 67P (Paquette et al. 2017 and 2018).

78
79 In addition to chemical information, COSIMA delivered images of the collected dust from the
80 built-in microscope camera COSISCOPE which enabled analysis of the dust flux and its time
81 evolution along the comet's trajectory inbound and outbound from the sun (Merouane et al.
82 2016 and 2017). The images further revealed that the collected dust particles are agglomerates
83 made up of smaller subunits (Langevin et al. 2016). An analysis of the fragmentation caused by
84 the impact at collection led to the conclusion that, in many cases, those subunits possess a
85 mechanical stability of their own and therefore have been denoted as „elements“ (Hornung et al.
86 2016). Atomic force microscope analysis from the MIDAS instrument onboard Rosetta (Bentley
87 et al. 2016, Mannel et al. 2016) suggested that these elements have further substructures on
88 the submicron scale. Optical scattering studies revealed volume scattering on the scale of the
89 elements and that the dust has high transparency and likely high porosity (Langevin et al. 2017).

90
91 The collected dust particles turned out to have low electrical conductivity such that those
92 elements of the agglomerate, which are located within the footprint of the spectrometer's
93 primary ion beam ($8\text{ kV } In^+$), can be positively charged. Small displacements of the elements
94 were often detected in the images taken immediately after the spectra acquisition. The charging
95 could even lead to fragmentation of larger particles which survived the impact at collection

96 undamaged, as has been shown by dedicated in situ experiments (Hilchenbach et. al, 2017).
97 The fragment size distribution due to the Lorentz forces, induced by charging, was almost
98 identical to the case of impact fragmentation, i.e. two completely different physical fragmentation
99 mechanisms result in a similar outcome and the conclusion is that the elements are already
100 present in the incoming dust as separate entities. When the COSIMA operations began to focus
101 on negative mode mass spectra, an asymmetry in the line shapes was observed, consisting in a
102 large contribution preceding the main mass peak, expanding up to 10 times the width of the
103 main peak, which was still narrow and located at the expected mass position. This asymmetry
104 appears because the electrical potentials of COSIMA's time-of-flight section are distorted from
105 their optimum values, due to the charging of the dust particles, and we found that it reflects
106 information on the electrical properties of the dust. This information would have been lost by the
107 use of an electron gun to compensate the charging, which is usually the case in secondary ion
108 mass spectrometry operation in the laboratory. Such electrical properties, especially the real
109 part of the permittivity, can be used to derive limits on the dust's porosity. This method
110 represents a standard tool in geology (e.g. Rust et al. 1999) and it is also used when probing
111 the surface and subsurface areas of airless bodies in the planetary system, mostly by remote
112 radar techniques (e.g. Campbell and Ulrichs 1969, Boivin et al. 2018, Hickson et al. 2018).
113 During Rosetta's lander Philae operation in November 2014, the radiowave transmission
114 instrument CONSERT and the impedance probe SESAME-PP derived the porosity of the
115 comet's subsurface from electrical permittivity data, the former by radio waves crossing the
116 comet nucleus, and the latter injecting an AC current in the low frequency range at the landing
117 near-surface (Kofmann et al. 2015, Herique et al. 2017, Lethuillier et al. 2016).

118

119 The present report analyzes the line asymmetry observed in COSIMA's negative secondary ion
120 mass spectra with the goal to derive electrical properties, and from this an estimate of the
121 porosity of the dust's elements. Sec. 2 briefly introduces the reader to the problem by giving

122 details of the physical environment on the collection targets on which the dust is trapped,
123 showing examples of the asymmetrical line shapes and reporting on tests with COSIMA's
124 laboratory model („reference model, RM“). Sec. 3 presents a numerical scheme to calculate the
125 line profiles by modelling the relevant line broadening mechanisms with open parameters, to be
126 fitted to COSIMA's flight spectra. Since it has been observed that the charging reaches a
127 limiting value after less than a second, a current must flow in the stationary state from the
128 charged elements to the grounded target. In Sec. 4 this treatment is applied to the COSIMA
129 negative mode mass spectra and values for the model parameters are derived, the charging
130 potential being the most important one. Further technical details are provided in the Appendix.
131 The implications for the comet's dust electrical properties are then discussed in Sec. 5. Based
132 on the findings on the charging potential and the kind of current conduction, a lower limit for the
133 specific resistivity of the elements is derived. Using a series of spectra acquisitions with
134 increasing exposure time gives an upper limit for the charge-up time. By combining with the
135 lower limit of the resistivity, an upper limit for the real part of the relative electrical permittivity at
136 direct-current conditions (DC) follows. This upper limit is then used to derive a lower limit for the
137 porosity of the dust's elements by applying known mixing rules, which determine the permittivity
138 of the porous matter from the corresponding values of the compact constituents.

139

140

141

142

143

144

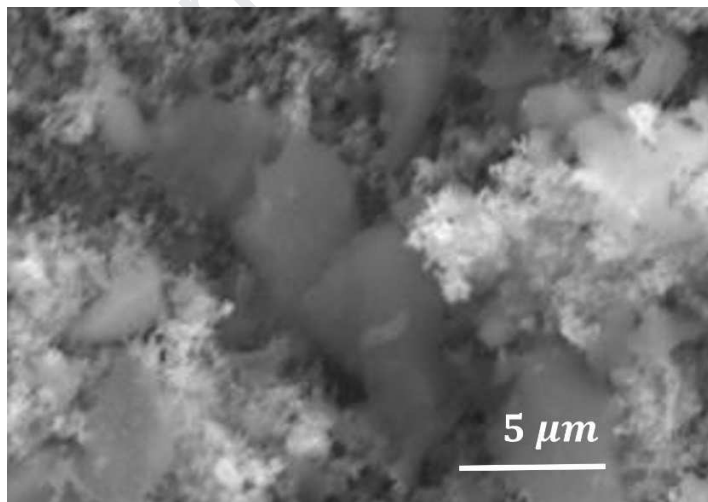
145

146 2. Observational data

147

148 2.1 Physical environment of the collected dust on the target

149 Dust particles from comet 67P were collected by impact onto $1 \times 1 \text{ cm}^2$ sized metal targets (Au or
150 Ag) covered with a 10 to 20 μm thick layer of a highly porous metal structure having grain sizes
151 of a few tens of nanometers. This layer is referred to as „metal black“ due to its deep black
152 appearance in visible light which provides an ideal background for optical inspection. The speed
153 of the incoming dust particles was a few m/s (Rotundi et al. 2015). Fig. 1 shows a SEM image
154 of a metal black structure with collected particles embedded in it from pre-flight laboratory
155 collection experiments (Hornung et al. 2014). The image illustrates what was expected prior to
156 the cometary encounter: many dust particles of micron size are dispersed amid the metal black
157 within the ion beam's footprint area (about $35 \times 50 \mu\text{m}^2$) such that the conductive target can

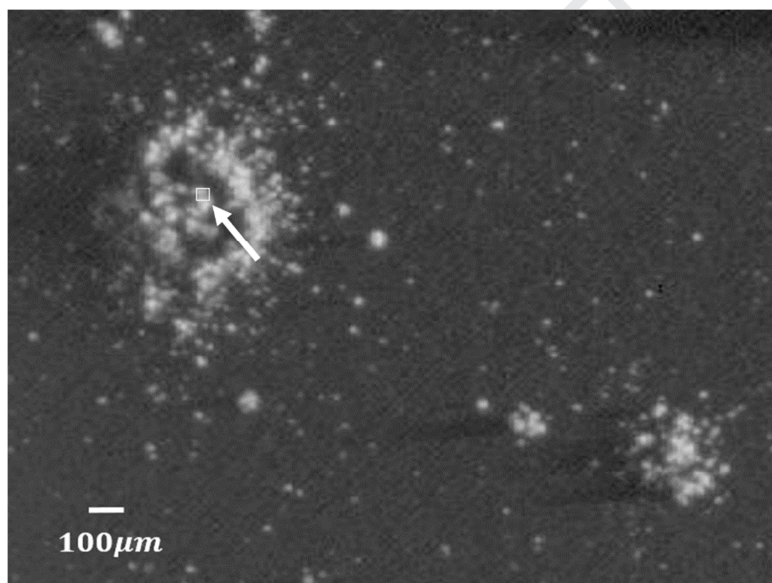


158 compensate possible charging of the dust particles.

159 Fig. 1. Pre-flight laboratory collection experiments: SEM image showing dust particles (dark
160 smooth areas) embedded in highly porous silver black (the fluffy and lighter material on the
161 image).

162

163 The reality at the comet turned out to be different. Fig. 2 shows a COSISCOPE image of 67P
164 dust particles collected on a gold black target at a resolution of about $10\ \mu\text{m}$ (by using the
165 resolution enhanced Nyquist mode, see Langevin et al. 2016), much lower than in the laboratory
166 SEM image of Fig. 1. The dust particles are larger than expected, a few $100\ \mu\text{m}$ up to $1\ \text{mm}$, as
167 seen by their lateral extent as well as their cast shadow. The image clearly shows the
168 agglomerate structure with subunits („elements“) having sizes of several tens of micrometers
169 such that a few of them may be located within the footprint of the primary ion beam.



170

171

172 Fig. 2. Dust particle Jessica (upper left), collected on the gold black target 2CF on Jan. 26,2015,
173 imaged Feb. 10, 2015 (white square: position of SIMS measurement). For naming conventions
174 see Langevin et al. 2016.

175

176

177

178 *2.2 Observation of asymmetrical line shapes in the COSIMA negative spectra*

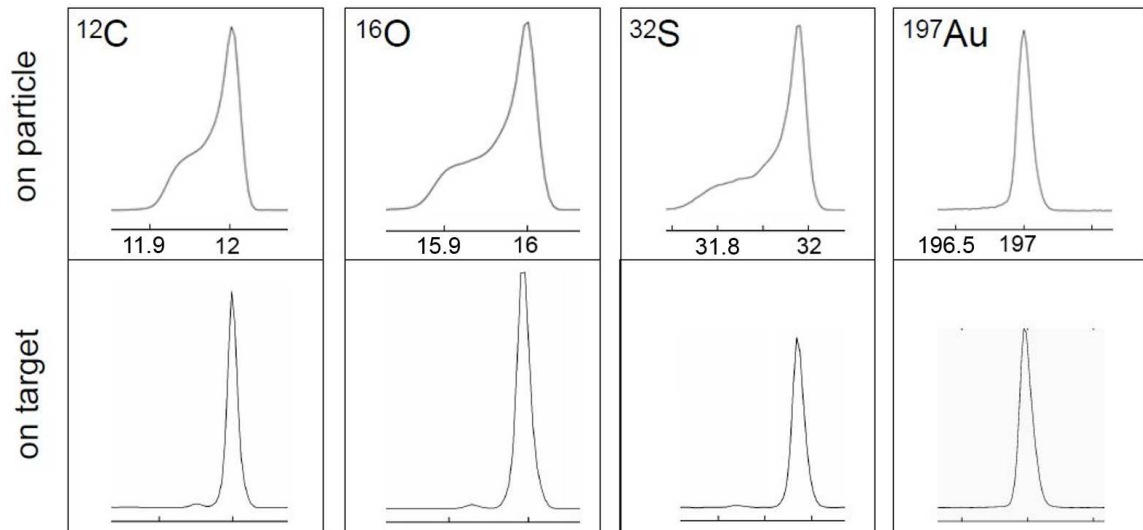
179 During the SIMS analysis of the collected dust particles, the spectra in negative ion mode
180 featured mass lines with shapes changing in a very peculiar way: Left from the line peak, i.e. at
181 lower mass values, there evolves a long signal extension which grows in intensity when the dust
182 particle gets increasingly into the focus of the ion beam. Generally asymmetries appear
183 whenever there is a deviation of the spectrometer's electrical potential settings from their
184 optimum design values. However, operational variations of the instrument settings could be
185 ruled out, since they were continuously measured and transmitted to ground together with every
186 spectrum and did not show any changes. It thus became obvious that surface charging was
187 building up on the dust particle, a known side effect in laboratory SIMS applications when the
188 probe has low electrical conductivity (Werner and Morgan 1976).

189

190 Fig. 3 shows examples for the mass lines ^{12}C , ^{16}O , ^{32}S and ^{197}Au measured at the dust particle
191 of Fig. 2. Due to their special shape we denote these profiles hereinafter as „left shoulder“
192 profiles. While most of the line profiles show this asymmetry, some do not, such as ^{197}Au , which
193 obviously originates from uncharged target areas which may remain within the focus of the
194 primary ion beam. In contrast, when the primary ion beam hits the gold black target only, all
195 lines show symmetric shapes. Due to the SIMS high detection sensitivity, even on these “empty”
196 parts of the gold black target one observes, besides gold, a multitude of lines from surface
197 contaminants, e.g. C, O and S .

198

199



200

201 Fig. 3. Upper panels: Asymmetrical TOF-SIMS line shapes in the negative ion mode mass
 202 spectra from particle Jessica on the gold black target 2CF, sum of 1001 spectra. Lower panels:
 203 Corresponding lines when the primary ion beam hits an empty gold black target position,
 204 located far from Jessica (about $4000 \mu\text{m}$), sum of 69 spectra. Linear vertical axis, arbitrary units.

205

206 2.3 Laboratory tests of charging with the COSIMA reference model

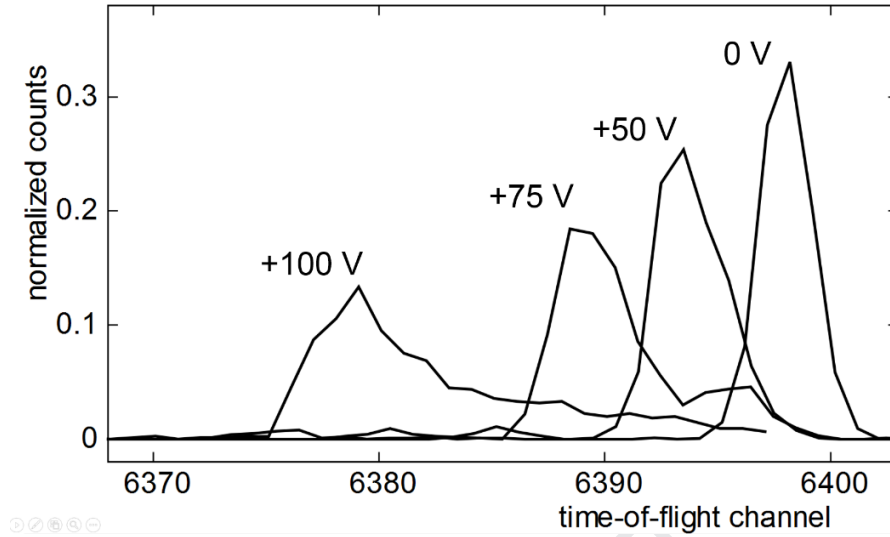
207 When the dust particle gets a positive bias with respect to the target due to charging, then
 208 negative secondary ions do not experience the full extraction voltage U_{EL} of the instrument (see
 209 Appendix), but a value reduced by the bias. In order to quantify the response of COSIMA to
 210 such a change, a series of mass spectra has been measured with the laboratory instrument of
 211 COSIMA ("reference model RM"). A target (a carbon strip from a commercial resistor) was set to
 212 various constant positive potentials. Fig. 4 shows the results for the example of the negative
 213 oxygen line. Depending on the value of the positive target potential, the $^{16}\text{O}^-$ line shifts as a
 214 whole towards earlier times (to lower mass). This shift means that negative ions desorbed from

215 positively biased targets arrive earlier at the detector, despite being slower as a result of the
216 reduced extraction voltage. This „reverse“ behaviour is due to the special two-stage reflectron
217 used (Mamyryn 2001). Fig. A1 of the Appendix shows the corresponding setup. Ions with lower
218 kinetic energy dive less deeply into the space between grids 4 and 5 than their companions with
219 higher speed and they leave this space earlier. In their further travel the faster ones cannot
220 catch up and finally the slower ones arrive earlier at the detector. The Mamyryn version has the
221 advantage of being “energy-focussing” when operating at its optimum voltage configuration, i.e.
222 it efficiently corrects the spread in the initial energy of the secondary ions at emission (a few
223 eV), achieving spectral lines with high mass resolution. However, it reacts very sensitively and
224 loses this capability when the extraction voltage deviates from its optimum due to charging. As
225 consequence, the profiles in Fig. 4 feature a large tail to the right, which becomes broader with
226 increasing charging potential (the tails shown in Fig. 4 are consistent with a Maxwellian
227 distribution having a characteristic energy of $U_0 = 5 - 10 eV$).

228

229 The RM tests clarified COSIMA’s reaction to a uniform charging level imposed by a fixed bias at
230 a conductive target. However, in the case of COSIMA’s flight data, where the charging is
231 produced by the primary ion beam, there is a continuum of charging potentials from zero up to a
232 maximum value, caused by the spatial Gaussian profile of the primary ion beam. Therefore, one
233 does not observe a shift of the whole line, but a broad continuum to the left, which represents a
234 superposition of left-shifted profiles of the kind shown in Fig. 4. It is interesting to note that Fig. 4
235 already gives a first estimate of the maximum shift of about 20 time bins for a charging of
236 $100 V$ for the case of oxygen ions, in agreement with the extent of the „left shoulder“ one
237 observes in COSIMA’s flight spectra.

238



239

240 Fig. 4. Negative ion mode mass spectra obtained with the COSIMA-RM laboratory model
 241 showing the left shift and the deformation of the $^{16}\text{O}^-$ line when the target is positively biased
 242 (time channel bin size= 1.956 nsec).

243

244 3. Modelling line shapes in the presence of charging

245 The empirical insights into the problem, as discussed up to now, allow us to establish a model to
 246 calculate the line shape. It is built upon several open parameters, which are then fitted to the
 247 COSIMA negative spectra. Within this model, the spectral amplitude $A(t)$ follows from a
 248 superposition of three major broadening contributions:

249

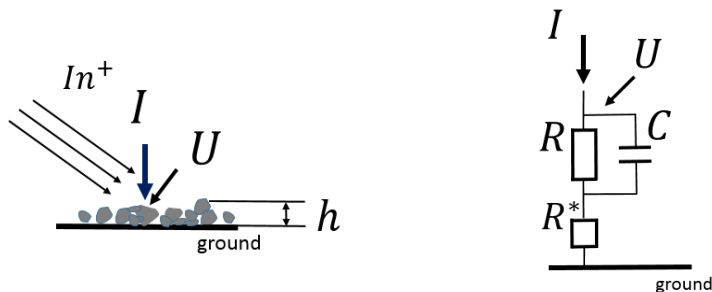
$$250 \quad A(t) = \int \delta(t - t_{det}(t_0, v_0, r)) \cdot f_t(t_0) \cdot f_v(v_0) \cdot f_r(r) dt_0 dv_0 dr. \quad (1)$$

251

252 δ is the delta function and t_{det} is the arrival time at the detector. The equation links the spectral
 253 amplitude $A(t)$, or in other words, the probability of a secondary ion to arrive at a time t at the
 254 detector, to the following variables : 1. The moment of generation at the target t_0 , its
 255 abundance $f_t(t_0)$ being represented by a Gaussian, which describes the time dependence of
 256 the primary ion pulse, 2. the initial emission velocity of the secondary ions (axial component), v_0
 257 , its abundance $f_v(v_0)$ being represented by a Maxwellian, 3. the radius r within the primary
 258 beam relative to the beam center (in the plane normal to the beam axis) from which the primary
 259 ion beam current density (ions per unit area and unit time), $i(r)$, depends via a Gaussian. The
 260 probability for a certain radius is then $f_r(r) = 2\pi r \cdot i(r) \cdot f_{tr}(U_c)$, where $f_{tr}(U_c)$ accounts for the
 261 transmission loss due to the charging potential $U_c(r)$ (see Appendix). $U_c(r)$ itself can be
 262 expressed as a function of $i(r)$ as will be discussed below. All three variables,
 263 (t_0, v_0, r) contribute to the broadening of the line and our finding is that they are sufficient to
 264 represent the most important features of the measured line shapes. The detector arrival time
 265 t_{det} is the sum of the generation time t_0 and the passage time t_{TOF} of the secondary ions
 266 through the time-of-flight section of the spectrometer: $t_{det}(t_0, v_0, r) = t_0 + t_{TOF}(v_0, r)$, and the
 267 way t_{TOF} is calculated is explained in the Appendix. The numerical solution of Eq. (1) uses
 268 discretized values of t_0, v_0 and r .The integration is performed using the same binning technique
 269 as the COSIMA electronics: a certain ion generated at time t_0 , having an initial velocity of v_0
 270 and starting from a location which is charged by some amount $U_c(r)$ is sent through the
 271 instrument and its arrival time t_{det} is sorted into an array of equally spaced bins for the variable
 272 t (bin size= 1 TOF unit). By sending a large number of ions (several 10^6) through the
 273 instrument, and adding up the counts that fall into each time bin, a discrete data set for the
 274 spectral amplitude $A(t)$ is generated.

275

276 The dust charging potential depends on the primary ion beam current and the dust's electrical
 277 properties (Werner and Morgan 1976). Suppose that the primary beam (8 keV positive ions of
 278 isotopically clean ^{115}In) hits a dust layer of height h of the agglomerate dust structure as shown
 279 schematically in Fig. 5. A certain surface area receives a current I and develops a potential
 280 difference $U(t)$ between top and bottom depending on the resistance R and capacity C of
 281 individual elements of the agglomerate (R^* accounts for a possible contact resistance between
 282 the bottom of the dust and the grounded target). The primary ion beam is pulsed with a
 283 repetition rate of 1.5 kHz, the pulse width Δt_p being a few ns, yet it acts as a DC current
 284 because the rise time τ of charging has been found to be on the order of a second. After this
 285 initial rise time the charging potential keeps a constant value U_c , which leads to the conclusion
 286 that a steady current must flow through the dust to the target during the spectra acquisition time
 287 of a few minutes. Although extremely small (in the order of 1/10 of a pA), this current is essential
 288 to maintain the charging of the dust. Thus the cometary dust particles are not insulators, but
 289 poor conductors and the electrical behaviour cannot be described by electrostatics alone. The
 290 initial rise time τ has no influence on the interpretation of the spectral line shapes and the
 291 measured values of the charging potential, U_c , always represent the asymptotic steady state
 292 limits. However, the rise time becomes important when discussing the dust permittivity in
 293 Section 5.



294

$$(U(t) = I \cdot R^* + I \cdot R \cdot (1 - e^{-t/\tau}); t \gg \tau: U(t) \rightarrow U_c = I \cdot (R + R^*); \tau = R \cdot C)$$

295 Fig. 5. Equivalent scheme for the buildup of the charging potential U .

296

297 The dependence of the steady state limit of the charging potential on the current density, which
 298 is caused by the primary ion beam, has to be determined from the shape of the spectral lines. At
 299 this point it should be noted, that the line shape does not depend on the absolute value of $i(r)$,
 300 but only on its radial distribution. However, the absolute value will come into play when
 301 discussing electrical properties below. With the maximum charging $U_{c,max}$ and the maximum
 302 current density i_{max} occurring at the center of the primary beam's footprint, the potential-current
 303 relationship can be formally written in a dimensionless form:

304

$$305 \frac{U_c(r)}{U_{c,max}} = \phi(y); \quad y = i(r)/i_{max} . \quad (2)$$

306

307 Several functions for the dependence of the reduced charging potential $\phi(y)$ on the reduced
 308 current density y have been tested resulting in the following empirical dependence with an open
 309 shape parameter ξ :

310

$$311 \phi_\xi(y) = \frac{\arctan(y/\xi)}{\arctan(1/\xi)} . \quad (3)$$

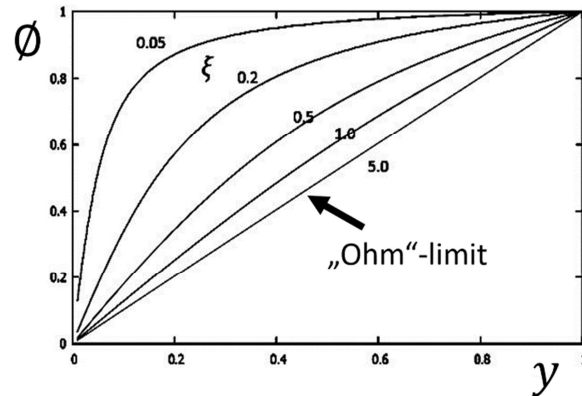
312

313 The physical significance of ξ becomes clear, when considering its limits as illustrated in Fig. 6.

314 For small values of ξ , already small currents cause a final saturation charging level $U_{c,max}$. In

315 this case, the width of the distribution of U_c values would be narrow. In the limit of $\xi \rightarrow 0$ there is

316 only one value for U_c (a spatially uniform charging caused by sideward charge transport) and
 317 consequently the spectral line is shifted to the left as a whole. In the limit of large ξ , potential
 318 and current are proportional ($\phi(y) = y$), which means „ohmic“ behaviour is present. The ansatz



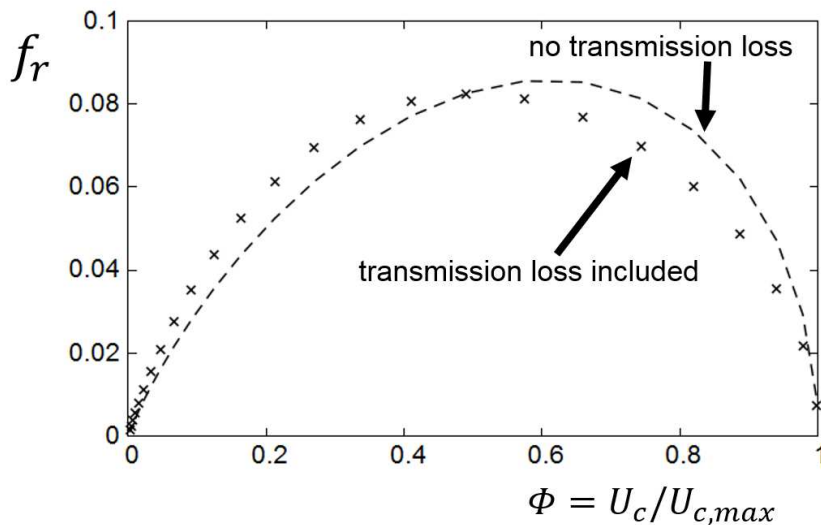
319 of Eq. (3) gives a possibility to formally include all possible situations between uniform charging
 320 and „ohmic“ behaviour and then derive from the spectra which case prevails.

321 Fig. 6. Dependence of the reduced charging potential $\phi(y)$ on the reduced current density y .

322

323 The contribution to the line profile from the charged areas can be interpreted as a weighted
 324 superposition of profiles shifted in time by an amount corresponding to the value of the charging
 325 potential U_c , where f_r is the weight function. Fig. 7 shows an example for f_r in the case of
 326 „Ohm's limit“: $\phi(y) = y$. The sharp decrease close to $\phi = 1$ is responsible for a characteristic
 327 cutoff of the line profile at its left end, as observed in the COSIMA flight spectra. COSIMA data
 328 analysis showed that there are cases when the primary ion beam does not only hit the dust
 329 particle, but partly also the target where no charging appears. Therefore an additional
 330 parameter is introduced, w_1 , describing the area fraction of uncharged material (the area fraction
 331 of charged material is then: $w_2 = 1 - w_1$). In addition, along with the negative ions, there is a
 332 small contribution to the spectral line coming from secondary electrons generated by ion impact
 333 onto a grid, located immediately before the detector (see Appendix, Fig. A.1, grid No. 8). These
 334 electrons produce a lower mass spectral feature, left from the ion contribution. Their fraction w_{el}

335 is a few percent of the total line integral as suggested by spectra on no-dust (target) positions
 336 (e.g. the lower panels, "on target" of Fig.3). The final line profile is obtained by adding up the
 337 contributions from uncharged and charged areas as well as secondary electrons, each
 338 calculated separately with the above described binning technique, and weighting them with
 339 w_1 , w_2 and w_{el} respectively. Both, the amplitudes of the model profile and the COSIMA spectral
 340 data, are then normalized to 1. This ensures that the line integrals of model and data are
 341 identical, giving freedom only for the shape of the profile. The model time t is finally converted
 342 into a mass value m via: $m = (t/a)^2$, where a is a parameter (sometimes called the „stretch
 343 parameter“), which depends on the instrument’s electrical potential settings. It is adjusted using
 344 the measured spectra. It turned out that all calculated times fall into a time-interval from about
 345 $13 \cdot \sqrt{M}$ time bins left from the line center to about $5 \cdot \sqrt{M}$ time bins right, which defines the time



346 window for the fit, the time bin unit being 1.956 nsec and M being the nominal mass number of
 347 the spectral line under consideration, for example $M = 15.9955$ for the oxygen isotope $^{16}\text{O}^-$.

348 Fig. 7. Probabilities for individual charging potential values for the case of $\phi(y) = y$. The
 349 example uses 25 values for the discretization and the transmission loss is for the example of
 350 $U_c = 100 \text{ V}$.

351

352 The spectral data are used in a rebinned version and the comparison between calculated and
353 measured line profiles is done on the mass scale. The rebinning process accounts for small
354 variations in the instrument status over time (e.g. potential values) which lead to small variations
355 in the position in time of the main known mass lines. The first step of the rebinning process is a
356 dead time correction of the spectra, followed by calibration and a final interpolation of the data
357 into a fixed time/mass scale. Only after such a procedure can many spectra be properly added
358 to improve statistics without introducing artificial broadening. However, by this procedure the
359 connection to the original time base of the instrument is lost, which means that now the
360 experimental input is always amplitude versus mass. The adjustable parameter a then makes
361 the connection between mass and the model time.

362

363 The evaluation of the 8 parameters (summarized in Table 1) is facilitated by the fact that each of
364 them has its largest influence only in certain parts of the profile. For example, the time width of
365 the primary beam pulse, Δt_p , is important close to the line maximum, but does not influence the
366 shoulder close to its left boundary whereas the maximum charging $U_{c,max}$ is important at the left
367 boundary, but not close to the line maximum. Our observation is that the parameters generally
368 do not show big variations, such that a good initial guess can be defined and the number of
369 iterations is small (typically 3 to 5). Some of the parameters can be easily estimated. For
370 instance, Δt_p can be inferred from ions originating from the target (typically 5 – 10 *nsec*). The
371 secondary electron fraction, w_{el} , cannot exceed a few percent, since the grids of the instrument
372 have a transparency of higher than 90 %. Initial energies of secondary ions are known to be on
373 the order of several *eV*, extending up to 5 – 25 *eV*. In the end, only three parameters with a
374 large influence remain: The shape parameter ξ , the maximum charging potential $U_{c,max}$ and the

375 fraction of ions from uncharged areas, w_1 (charged: $w_2 = 1 - w_1$). Therefore optimization begins
376 with these and then a fine-tuning of the others leads to a rapid convergence.

377

Journal Pre-proof

378

379 Table 1: Summary of parameters.

ξ	shape parameter of the charge function Eq. (3).
$U_{c,max}$	maximum charging at the footprint of the primary ion beam center (<i>Volt</i>).
U_{01}	Maxwell energy parameter uncharged areas (<i>eV</i>).
U_{02}	Maxwell energy parameter charged areas (<i>eV</i>).
Δt_p	pulse width (full width at half maximum) of the primary ion beam (<i>nsec</i>).
w_{el}	fraction of secondary electrons from grid 8 (see Appendix).
w_1	fraction of ions from uncharged areas (charged areas: $w_2 = 1 - w_1$).
a	stretch parameter (in units of $1.956 \text{ ns} / \sqrt{M}$).

380

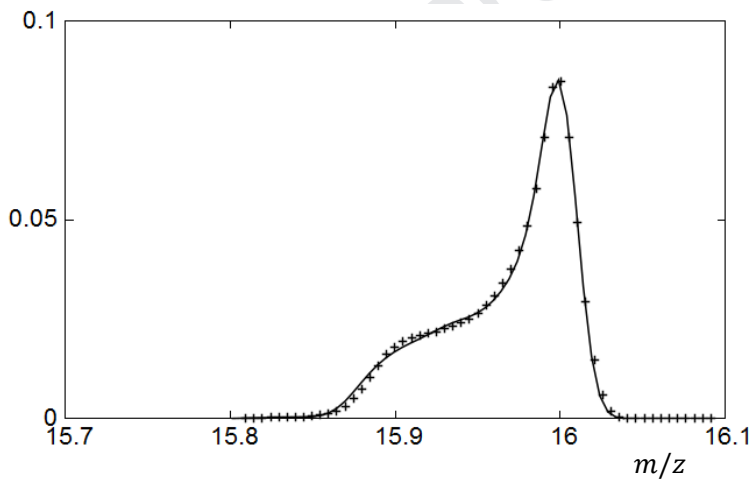
381

382 **4. COSIMA negative mode spectra**

383 The first example contains a very long measurement (≈ 48 h) on the dust particle Jessica on
384 target 2CF. A sum spectrum is used, consisting of a total of 1001 negative spectra acquired at 4
385 positions which are $30\mu\text{m}$ apart from each other (marked as the corners of a white square in Fig.
386 2). Jessica data show the most pronounced left shoulder of all measured particles. Fig. 8 shows
387 the individual data points (+) of the sum spectrum together with the model values (solid line) for
388 the oxygen line. To be correct, both curves of Fig. 8 are histograms, but plotted as points and

389 line for the sake of a clearer perception of the very small differences between data and model.
 390 The fit result shows that the shape parameter ξ is equal to 1, which is close to Ohm's limit. Fig.
 391 9 shows an example of a very wide left shoulder from particle Jakub corresponding to high
 392 charging potential. Since in this case the data are averaged over only a few individual spectra,
 393 fluctuations are present originating most likely from spatial variations in the dust coverage within
 394 the primary ion beam's footprint. Most of the ions originate from the charged dust particle in this
 395 example, i.e. a low value of w_1 . Fig. 10, particle Juliette, shows an example of an exceptionally
 396 narrow left shoulder corresponding to a maximum charging potential $U_{c,max}$ of only 67 V and it
 397 has a low charged fraction (high value of w_1).

398

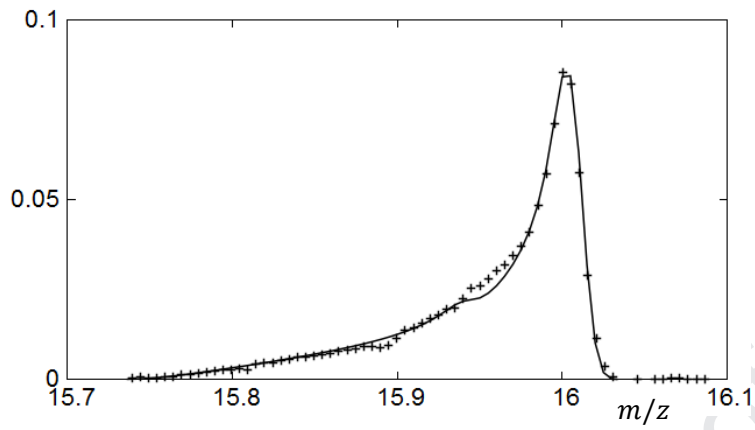


399

400 Fig. 8. Oxygen line profile: Normalized spectral amplitude (counts / total counts contributing to
 401 the oxygen mass line) versus m/z . Particle 2CF Jessica: +=spectral data, sum of 1001 spectra.
 402 Solid line: present model, Eq. (1). Parameters: $\xi = 1$, $U_{c,max} = 98 V$, $U_{01} = 10 eV$, $U_{02} =$
 403 $4 eV$, $\Delta t_p = 9 nsec$, $w_{el} = 0.02$, $w_1 = 0.23$, $M = 15.9955$, $a = 1601.3$.

404

405

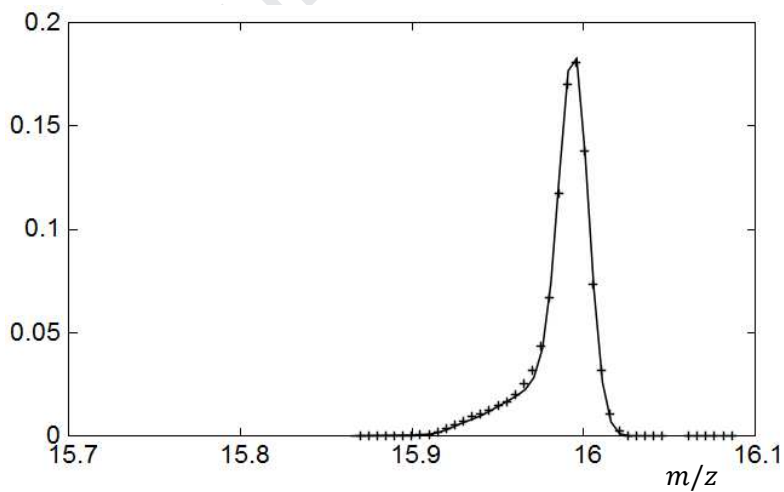


406

407

408 Fig. 9. Oxygen line profile, example: high charging potential: Particle 2D1 Jakub: +=spectral
409 data, sum of 10 spectra. Parameters: $\xi = 5$, $U_{c,max} = 129 V$, $U_{01} = 10 eV$, $U_{02} = 10 eV$, $\Delta t_p =$
410 $6 nsec$, $w_{el} = 0.04$, $w_1 = 0.03$, $M = 15.9955$, $a = 1601.0$.

411



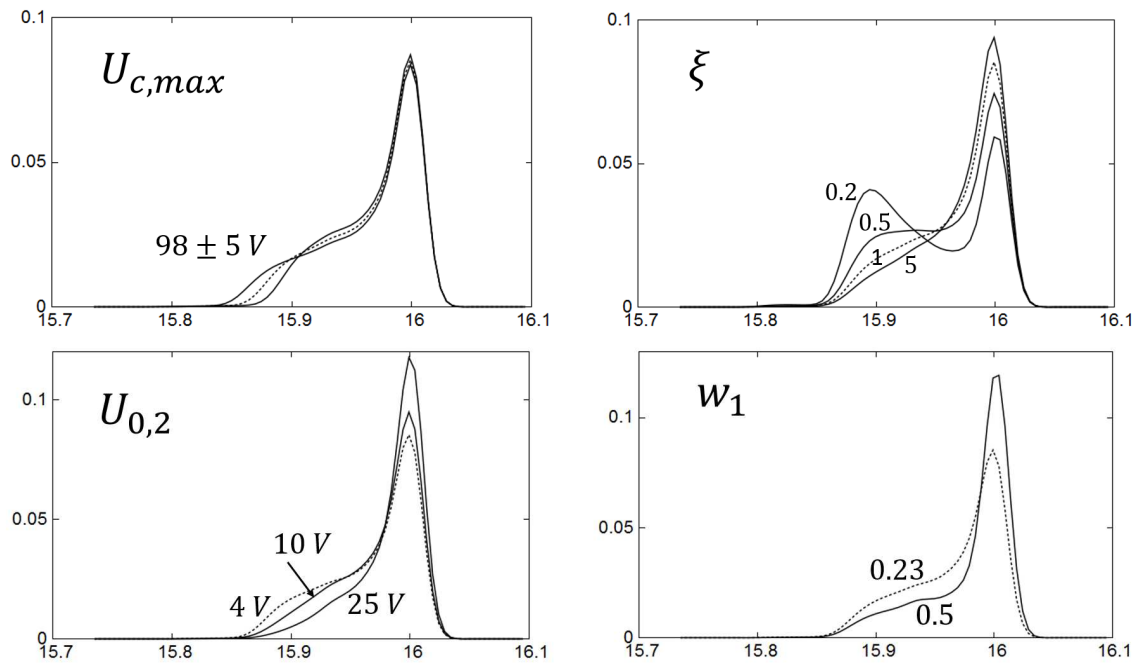
412

413

414 Fig. 10. Oxygen line profile, example: low charging potential and low charged fraction: Particle
415 1D2 Juliette: +=spectral data, sum of 12 spectra. Parameters: $\xi = 2$, $U_{c,max} = 67 V$, $U_{01} =$
416 $10 eV$, $U_{02} = 5 eV$, $\Delta t_p = 7.5 nsec$, $w_{el} = 0.02$, $w_1 = 0.70$, $M = 15.9955$, $a = 1601.7$.

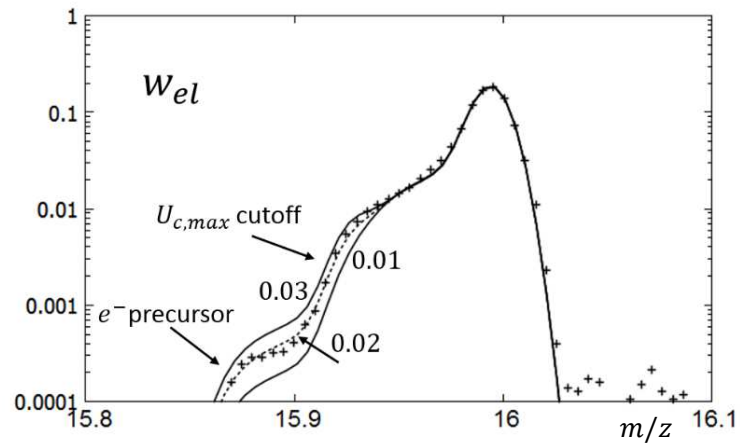
417

418 To demonstrate how sensitive the results are to changes in the individual parameters, Fig. 11
419 contains parameter variations for the example of Fig. 8. It shows that the maximum charging
420 potential $U_{c,max}$ determines the left cutoff of the shoulder and the dependence is very sensitive,
421 i.e. a few Volts difference yields in a significant difference. Large variations in the shape
422 parameter ξ would deform the profile in a way which is not observed in the data. Variations of a
423 few eVs in the emission energy U_{02} of the charged areas causes a characteristic change in the
424 line shape. Variations in the uncharged fraction parameter w_1 do not influence the shape of the
425 left shoulder, but its vertical level. Although the contribution to the spectral signal resulting from
426 the secondary electrons is only a few percent, it is in some cases significant to recognize the left
427 end of the shoulder. Fig. 12 shows variations of w_{el} for the example of 1D2 Juliette in
428 logarithmic scale to better recognize details of the left end of the profile. The main cutoff is
429 connected to the maximum charging and the electron signal occurs before it, since the electrons
430 (in Fig. 12 denoted by „ e^- precursor“) arrive earlier at the detector plate than the ions which
431 caused them. The figure also shows that the model of Eq. (1) represents the data over 3 orders
432 of magnitude down to the noise level.



433

434 Fig. 11. Parameter variations around the profile of 2CF Jessica (dotted line: fit of Fig. 8).



435

436

437 Fig. 12. Variation of the electron contribution w_{el} for the example of 1D2 Juliette (+ =

438

spectral data, dotted line: best fit; $w_{el} = 0.02$).

439

440 More example particles have been investigated with the present procedure. Table 2 contains
441 their reference data and the results of the corresponding fits are summarized in Table 3. In all
442 cases high values for the shape parameter were found: $1 \leq \xi \leq 5$. This means that the charge
443 transport is close to the case of an Ohmic resistor. The initial kinetic energy of the ions U_{01}
444 originating from non-charged areas has little influence on the left shoulder structure, whereas
445 the initial kinetic energy of the ions from the charged areas, U_{02} , enters significantly. Here, one
446 has to recall that the model introduced Maxwellian distributions of the axial component of the
447 emission velocity because the exact angular emission characteristics of the secondary ions is
448 hard to define for a surface of high and unknown roughness. Low values (particles Jessica and
449 Juliette) may correspond to more diffuse emission leading to small contributions in axial
450 direction. The division into charged and uncharged fractions, characterized by w_1 , shows large
451 variation, between 0 and 70%. This is especially an issue when using the present scheme for
452 later interpretations of negative spectra. The fit parameters of Table 3 are for the ^{16}O peak. For
453 the particles Juliette, Gunter and Jakub, the corresponding parameters for ^{32}S are added to give
454 an idea about mass number dependences. In the case of Juliette, sulfur seems to originate in
455 less proportion from target areas compared to oxygen as can be seen from the lower value of
456 the uncharged fraction w_1 . Emission energies U_{02} from charged dust areas might be dependent
457 on the ion species (e.g. Juliette and Gunter). The table contains, in addition to the fit
458 parameters, the values for the mean height h of the particle layer at measurement position as
459 estimated from the cast shadow at images taken after the SIMS analysis. They show an
460 increase of the charging potential with height.

461

462

463

464

465

466 Table 2: Reference data for the spectra used (sum of N individual spectra, each with an
 467 acquisition time of 2.5 minutes; for naming conventions see Langevin et al. 2016).

Particle name	Collection start date	N	SIMS analysis date
2CF Jessica Lummene.2	2015/01/26	1001	2016/04/01- 2016/04/04
1CD Barmal Orivesi.4	2015/07/31	8	2015/08/13
1D2 Juliette Hankavesi.1	2015/10/23	12	2015/11/18
1D2 Gunter Jerisjarvi.1	2016/02/29	96	2016/04/14
2D1 Jakub Toivesi.2	2015/05/11	10	2015/06/12
2D1 David Toivesi.2	2015/05/11	6	2015/06/12
2D1 Sora Ukonvesi.4	2015/05/22	12	2015/06/17

468

469

470 Table 3: Summary of fit results for 7 particles for the $^{16}\text{O}^-$ profile (upper line) and for 3 examples
 471 of the $^{32}\text{S}^-$ profile (lower line). w_1 is the fraction of ions from uncharged areas. h : dust layer
 472 height at SIMS position. The unit of the stretch factor a is $1.956 \text{ ns}/\sqrt{M}$, where M is the mass
 473 number of the line profile under consideration.

Target- and particle name	ξ	$U_{c,max}$ [V]	U_{01} [eV]	U_{02} [eV]	Δt_p [nsec]	w_{el}	w_1	a	h [μm]
2CF Jessica	1	98	10	4	9.0	0.02	0.23	1601.3	35
1CD Barmal	5	95	10	20	7.0	0.01	0.65	1601.6	35
1D2 Juliette	2	67	10	5	7.5	0.02	0.70	1601.7	18
	2	67	10	10	7.5	0.03	0.35	1601.6	
1D2 Gunter	5	130	10	25	7.0	0.04	0.01	1601.5	57
	5	130	10	20	7.0	0.04	0.00	1601.5	
2D1 Jakob	5	129	10	10	6.0	0.04	0.03	1601.0	55
	5	129	10	10	6.0	0.04	0.01	1601.2	
2D1 David	1	80	10	10	7.0	0.02	0.75	1601.6	20
2D1 Sora	2	100	10	10	6.0	0.02	0.50	1601.6	34

474

475 The present model considers a homogeneous target for which the probabilities of individual
 476 potentials $U_c(r)$ only depend on the spatially varying current density $i(r)$ of the primary beam.

477 This is the reason why averaged spectra are used since spatial variations in the dust properties
 478 and morphology are damped when the primary beam slightly shifts during the SIMS scan of the
 479 dust particle. As mentioned above, particle Jakub (Fig. 9) is an example for such variations
 480 when only few spectra have been added. This structural effect becomes even more apparent for
 481 single spectra. We expect information on the morphological structure hidden in these spectra.

482

483

484 **5. Information on electrical properties of the collected cometary dust**

485 We have found that the cometary dust material when subject to a current, caused by the
 486 primary ion beam, acts like an ohmic resistor since the potential U_c is approximately
 487 proportional to the local current density i . The very close agreement between the line shape
 488 fits and COSIMA's flight spectra assures the reliability of the method and that it represents a
 489 direct way to measure this potential. The maximum charging potential $U_{c,max}$ varies with the
 490 height h of the dust layer, an information that can be used to derive the specific resistivity.
 491 Figure 13 shows that the values of Table 3 follow a linear dependence with an offset U_{off} of
 492 about 45 V, likely being due to an interface contact resistance between dust material and metal
 493 black. Then the specific resistivity ρ_r can be expressed as:

494

$$495 \quad \rho_r = \frac{U_{c,max} - U_{off}}{h} \cdot \frac{A_f}{I_{tot}} = b \cdot \left(\frac{A_f}{I_{tot}} \right), \quad (4)$$

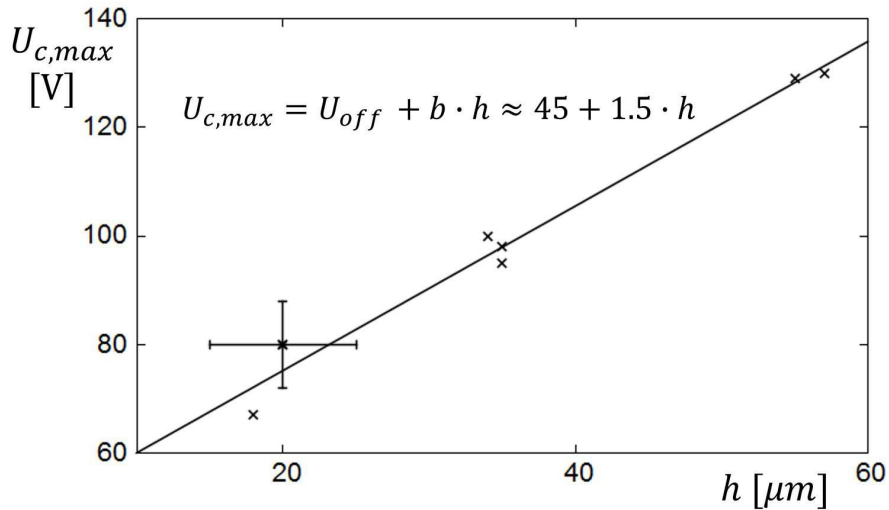
496

497 where A_f is the footprint area of the primary ion beam and I_{tot} is the total current, induced by the
 498 primary ion beam. The specific resistivity ρ_r can be derived either from the slope b of the fit in
 499 Fig. 13 or from individual pairs $U_{c,max}, h$. For the COSIMA flight model, I_{tot} has been estimated

500 to be $I_{tot} < 1.2 \cdot 10^{-13} A$ (Hilchenbach et al., 2017). Additional tests with the COSIMA reference
501 model („RM“) have been carried out in order to validate this value. The setup consisted of an
502 electrically insulated Au metal target and an oscilloscope (capacity target-ground 300 pF and
503 50 MOhm oscilloscope probe resistance). After an exposure to the primary ion beam of 2 min ,
504 the target was discharged via the oscilloscope probe and the total collected charge was derived
505 from the initial discharging voltage. The measured total current, as sum of the primary ion beam
506 and the induced secondary electrons, was in line with the current value referred above. It thus
507 provides an upper limit, since on the Au target the secondary electron yield is higher than on the
508 cometary dust material. The footprint area A_f has been determined experimentally to about
509 $1750 \mu m^2$. From the slope b of the fit line and the above values, a numerical value for the
510 resistivity of $\rho_r \approx 2.2 \cdot 10^{10} \Omega m$ results, which would characterize the cometary material as a
511 bad conductor, but not the best insulator. It is close to that of glass ($\approx 10^{10}$ - $10^{12} \Omega m$), but less
512 than that of e.g. Polyethylene ($\approx 10^{13} \Omega m$), Teflon ($\approx 10^{14} \Omega m$) or Polystyrene and Sulfur
513 ($\approx 10^{16} \Omega m$), (Chanda 2018). The asymptotic standard error of the fit line for each of the
514 parameters, U_{off} and slope b , is $\approx 10\%$ and there is a systematic uncertainty of up to $\pm 10 V$ in
515 the $U_{c,max}$ values and about $\pm 5 \mu m$ in the h values (in Fig. 13, the corresponding error bars are
516 shown only for one example to simplify the figure). Together with a 10% uncertainty in the beam
517 footprint area A_f , the combined maximum error is estimated to be $\pm 1.0 \cdot 10^{10} \Omega m$. Taking into
518 account that the value for I_{tot} forms an upper limit, the conclusion for the specific resistivity as
519 derived from the present data analysis is a lower limit: $\rho_r > 1.2 \cdot 10^{10} \Omega m$.

520

521

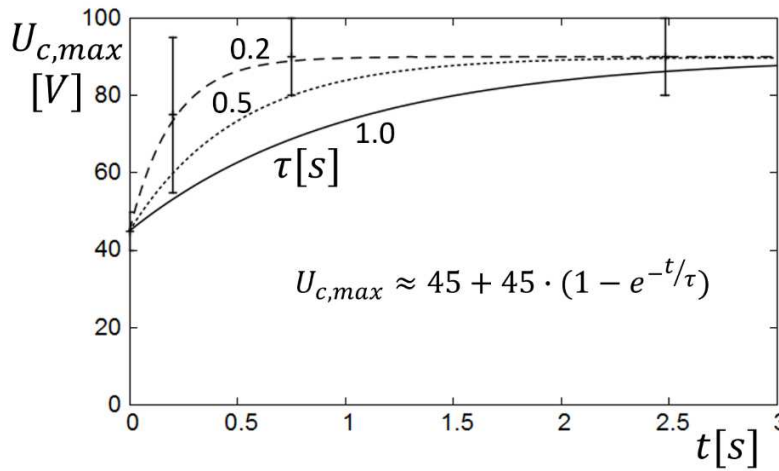


522

Fig. 13. Maximum charging potential vs. dust layer height.

523

524 Further information on dust charging comes from the build-up time $\tau = R \cdot C$ of the charge at the
 525 agglomerate's elements. Experimental information on τ has been obtained from *in situ*
 526 experiments at particle Lou on target 1C3. Spectra have been taken with sampling times of
 527 0.2, 0.75, 2.5, 9.5, 38 and 150 *sec* respectively with about one hour breaks in between to ensure
 528 decharging (Hilchenbach et al. 2017). The finding is that the 2.5 *sec* spectrum already shows a
 529 left shoulder with the asymptotic $U_{c,max}$ value at longer sampling times. From this one concludes
 530 that the $R \cdot C$ rise time τ has to be less than 1 *sec* (see Fig. 14).



531 Fig. 14. Dependence of charging potential on spectra sampling time for particle 1C3 Lou.

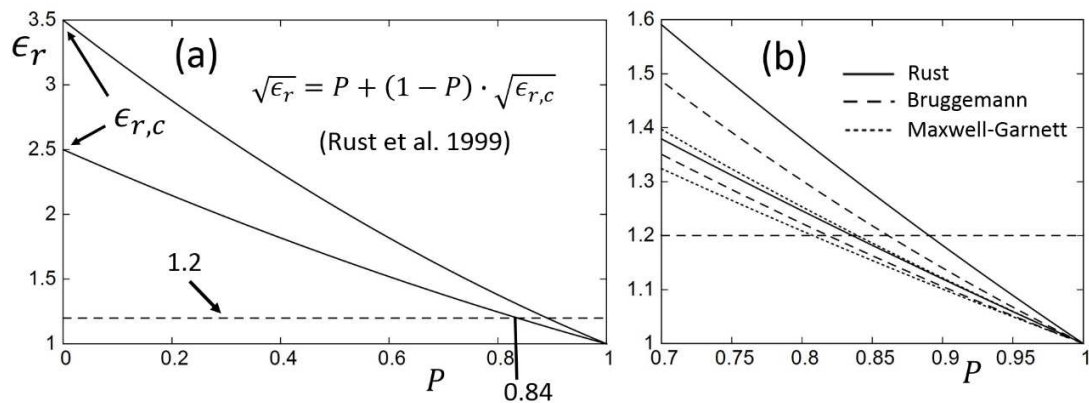
532

533 This information, together with the specific resistivity ρ_r , now allows us to derive the real part of
 534 relative permittivity ϵ_r for the elements of the dust agglomerate. For an estimate, assume them
 535 to be spherical (with radius \bar{r}), having a capacitance $C \approx 4 \cdot \pi \cdot \epsilon_r \cdot \epsilon_0 \cdot \bar{r}$ and a resistance
 536 $R \approx \rho_r \cdot 2 \cdot \bar{r} / (\pi \cdot \bar{r}^2)$ where ϵ_0 is the vacuum permittivity. Then the charge-up time becomes
 537 size-independent: $\tau \approx 8 \cdot \epsilon_r \cdot \epsilon_0 \cdot \rho_r$ and $\epsilon_r \approx \tau / (8 \cdot \epsilon_0 \cdot \rho_r)$. When considering other shapes
 538 than spheres the result does not change much. For instance in the case of a cube (Wintle 2004)
 539 one obtains $\epsilon_r \approx \tau / (8.3 \cdot \epsilon_0 \cdot \rho_r)$. From the measured upper limit of τ and the lower limit of ρ_r an
 540 upper limit for the relative permittivity follows: $\epsilon_r < 1.2$.

541

542 A value of ϵ_r so close to 1 is typical for high porosity materials and one can use this result to
 543 estimate the porosity. This estimate uses data on composition and typical permittivities of the
 544 main dust constituents, making use of the effective medium approach for mixtures. Rust et al.
 545 (1999) have measured a series of dry volcanic rocks and found the data fitting into an empirical
 546 law: $\sqrt{\epsilon_r} = P + (1 - P) \cdot \sqrt{\epsilon_{r,c}}$, where $\epsilon_{r,c}$ is the value of the corresponding compact material and
 547 P is the porosity. This power-law with exponent 1/2 is known as the Birchak equation (Birchak

548 et al.1974) and has been widely used in optics and refractive index models. In practice, there
 549 are several mixing rules based on empirical data and physical principles, such as the well-
 550 known Maxwell-Garnett (1904) and Bruggeman (1935) formulae, along with power-law fits with
 551 typical exponents 1/2 and 1/3 (Maron and Maron 2008). Yet, all these models predict similar
 552 results for high porosity (Sihvola 2000). For the application of those mixing concepts one needs
 553 an estimate of the corresponding compact values. The composition data of the dust collected by
 554 COSIMA show that it has a mineral-to-organic ratio of $\approx 0.55/0.45$ by weight (Bardyn et al.
 555 2017). For the electrical properties one needs this ratio by volume, which is $\approx 0.3/0.7$ when
 556 assuming a density ratio mineral/organic of ≈ 3 (Greenberg and Li 1999). The organic part of
 557 the investigated particles is found to have high molecular weight (Fray et al. 2016) and typical
 558 permittivities for such materials are $\epsilon_{r,c} \approx 2$ (Chanda 2018). Mineral values show a greater
 559 variety ranging from ≈ 4 (Silica) up to ≈ 8 (Olivine) and ≈ 8.5 (Pyroxene), (e.g. Zheng et al.
 560 2005).



561

562 Fig. 15. Real part ϵ_r of the relative electrical permittivity in dependence on the porosity P . (a):
 563 Rust's law, (b) details for high porosity and comparison with other mixing models (Bruggeman
 564 and Maxwell-Garnett multiphase).

565

566 Using the above mineral/organic by-volume ratio, a range of $2.5 < \epsilon_{r,c} < 3.5$ is estimated for the
567 compact dust mixture following Rust's mixing concept and Fig. 15a shows the corresponding
568 dependence on porosity. One can see that an upper limit of the permittivity $\epsilon_r = 1.2$ implies a
569 lower limit for the porosity: $P = 0.84$. Allowing for uncertainty in Rust's law, which seems to give
570 a slight overestimate compared to other models, Fig.15b, we finally estimate for the lower limit
571 of the porosity of the agglomerate's elements a value of 0.8.

572

573 6. Discussion and summary

574 During mass spectrometric analysis we observed dust particle positive charging, reaching
575 maximum values at the center of the primary ion beam's footprint and decreasing radially due to
576 the Gaussian beam profile. In negative ion mode it leads to a characteristic line shape with
577 extended left-shifted contributions („left shoulder“) while in positive ion mode it leads to a very
578 small shift of the line peak of typically few *nsec* and a substantial decrease in transmission since
579 those parts of the exposed area exceeding a charging limit of about 90 V cannot pass the
580 reflectron of the spectrometer. Within the present contribution we focussed on the negative
581 spectra. For a quantitative evaluation of the line asymmetry it is essential to recognize that the
582 left shoulder extensions fully contribute to the total line integral of the spectral mass line under
583 consideration and are not caused by neighbouring mass lines. The fact was already considered
584 in recent COSIMA papers (Fray et al. 2017, Bardyn et al. 2017, Paquette et al. 2017). We could
585 show that, after some initial build-up time, the potential at the dust is determined by a steady
586 DC-like current, approximately following Ohm's law and explicit values for the charging potential
587 could be extracted from the spectra (up to about 130 V for the examples discussed). These
588 charging potentials opened the possibility to derive information on the dust's electrical
589 properties. A lower limit for the electrical resistivity of 67P dust particles could be derived
590 ($\rho_r > 1.2 \cdot 10^{10} \Omega m$). When combining with a measurement of the charge build-up time ($\tau < 1 s$),

591 an upper bound for real part of the relative permittivity ϵ_r could be deduced which turned out to
592 be close to 1 ($\epsilon_r < 1.2$) and therefore indicating a high porosity of the dust particles ($P > 0.8$).
593 These values refer to dust's subunits (denoted by „elements“) with sizes approximately between
594 15 and 40 μm since the footprint of the primary ion beam is limited to an area of about 50 μm
595 diameter such that it contains only few elements. The CONSERT instrument on Rosetta
596 reported as well the observation of low values for the permittivity ($\epsilon_r = 1.27 \pm 0.05$) and high
597 porosity ($P = 0.75 - 0.85$) of the cometary interior tracked in the radio frequency region
598 (Kofmann et al. 2015, Herique et al. 2016). The SESAME instrument measurements on the
599 landing near-surface retrieved a maximum permittivity of 3 and a maximum conductivity of
600 $4 \cdot 10^{-8} (\Omega m)^{-1}$ and explained that with a weathered and sintered surface layer as well as ice
601 content (Lethuillier et al. 2016). For the material collected by COSIMA in the comet's coma, a
602 low permittivity value supports the assumption that the dust particles contained only minimal
603 water or ice after collection and storage within COSIMA for a few days to more than one year as
604 the DC relative permittivity of water or ice is much higher than that of minerals or organics (up to
605 values around 100, e.g. Aragoes et al., 2010, Pettinelli et al. 2015) and even tiny amounts of
606 them would increase the relative permittivity considerably (Strangway et al.1972, Anderson
607 2008). A high porosity of the collected cometary dust particles is also in line with our findings on
608 the strength, derived from the evaluation of the fragmentation dynamics upon collection
609 (Hornung et al. 2016) as well as on the optical properties, which include high transparency
610 values with a mean free path of the photons of about 20 – 25 μm within the dust particle
611 (Langevin et al. 2017).

612

613

614

615

616 Acknowledgments:

617 COSIMA was built by a consortium led by the Max-Planck-Institut für Extraterrestrische Physik,
618 Garching, Germany in collaboration with Laboratoire de Physique et Chimie de l'Environnement
619 et de l'Espace, Orléans, France, Institut d'Astrophysique Spatiale, CNRS/Université Paris Sud,
620 Orsay, France, Finnish Meteorological Institute, Helsinki, Finland, Universität Wuppertal,
621 Wuppertal, Germany, von Hoerner und Sulger GmbH, Schwetzingen, Germany, Universität der
622 Bundeswehr München, Neubiberg, Germany, Institut für Physik, Forschungszentrum
623 Seibersdorf, Seibersdorf, Austria, Institut für Weltraumforschung, Österreichische Akademie der
624 Wissenschaften, Graz, Austria and is lead by the Max-Planck-Institut für
625 Sonnensystemforschung, Göttingen, Germany. The support of the national funding agencies of
626 Germany (DLR, grant 50 QP 1801), France (CNES), Austria (FWF, grant P26871-N20), Finland
627 and the ESA Technical Directorate is gratefully acknowledged. We thank the Rosetta Science
628 Ground Segment at ESAC, the Rosetta Mission Operations Centre at ESOC and the Rosetta
629 Project at ESTEC for their outstanding work enabling the science return of the Rosetta Mission.

630

631 References

- 632 Anderson O. 2008. Dielectric relaxation of the amorphous ices. *J. Phys. Condens. Mater.* 20,
633 244115. doi:10.1088/0953-8984/20/24/244115.
- 634 Aragoes J.L. et al. 2010. Dielectric Constant of Ices and Water: A Lesson about Water
635 Interactions. *J. Phys. Chem. A*, 2011, 11523, 5745-5758. <https://doi.org/10.1021/jp105975c>.
- 636 Bardyn A. et al. 2017. Carbon-rich dust in comet 67P/Churyumov-Gerasimenko measured by
637 COSIMA/Rosetta. *Monthly Notices of the Royal Astronomical Society*, 469, S712-S722, DOI:
638 10.1093/mnras/stx2640.

- 639 Bentley M.S. et al. 2016. Aggregate dust particles at comet 67P/Churyumov–Gerasimenko.
640 *Nature* volume 537, pages 73–75. DOI: 10.1038/nature19091.
- 641 Birchak J. R. et al. 1974. High dielectric constant microwave probes for sensing soil moisture.
642 *Proc. IEEE*, Vol. 62, 1, 93–98. Doi: 10.11099/proc.1974.9388.
- 643 Boivin A.L. et al. 2018. Broadband Measurements of the Complex Permittivity of Carbonaceous
644 Asteroid Regolith Analog Materials. *Journal of Geophysical Research: Planets*, 123.
645 <https://doi.org/10.1029/2018JE005662>.
- 646 Bruggeman D.A.G. 1935. Berechnung verschiedener physikalischer Konstanten von
647 heterogenen Substanzen. 1. Dielektrizitätskonstanten und Leitfähigkeiten der Mischkörper aus
648 isotropen Substanzen. *Annalen der Physik*. 5. Folge. Band 24, pp. 636-664. doi:
649 10.1002/andp.19354160705.
- 650 Campbell M.J. and Ulrichs J.R. 1969. Electrical properties of rocks and their significance for
651 lunar radar observations. *J. Geophys. Res.* 74, 25, pp 5867-5881.
652 <https://doi.org/10.1029/JB074i025p05867>.
- 653 Chanda M. 2018. *CRC Handbook of Plastics Technology*, 5th Ed. CRC Press, ISBN 13: 978-1-
654 4987-8621-8, pp. 369 - 371. doi/10.1201/9781315155876-3.
- 655 Dahl D.A. 1997, INEEL, Idaho Falls, Idaho 83415, *The SIMION software manual*, 1997 (and
656 later versions).
- 657 Fray N. et al. 2016. High-molecular-weight organic matter in the particles of comet
658 67P/Churyumov-Gerasimenko. *Nature* volume 538, pages 72–74 (06 October 2016).
659 <https://doi.org/10.1038/nature19320>.
- 660 Fray N. et al. 2017. Nitrogen to carbon atomic ratio measured by COSIMA in the particles of
661 comet 67P/Churyumov-Gerasimenko. *Monthly Notices of the Royal Astronomical Society*.
662 doi.org/10.1093/mnras/stx2002.

- 663 Greenberg J. M., Li A. 1999. Morphological Structure and Chemical Composition of Cometary
664 Nuclei and Dust. *Space Science Reviews* 90: 149–161. doi: 10.1023/a:1005298014670.
- 665 Herique A. et al. 2017. Cosmochemical implications of CONSERT permittivity characterization
666 of 67P/CG. *Month Not. Roy. Astr. Soc.* Volume 462, Issue Suppl_1, 16 November 2016, Pages
667 S516–S532. <https://doi.org/10.1093/mnras/stx040>.
- 668 Hickson D. et al 2018. Near surface bulk density estimates of NEAs from radar observations
669 and permittivity measurements of powdered geologic material. *Icarus* 306, Pages 16-24.
670 <https://doi.org/10.1016/j.icarus.2018.01.018>.
- 671 Hilchenbach M. et al. 2016. Comet 67P/Churyumov–Gerasimenko: Close-up on Dust Particle
672 Fragments. *The Astrophysical Journal Letters* 816 L32. DOI: 10.3847/2041-8205/816/2/L32.
- 673 Hilchenbach M. et al. 2017. Mechanical and electrostatic experiments with dust particles
674 collected in the inner coma of comet 67P by COSIMA onboard Rosetta. *Phil. Trans. R. Soc.*
675 *A375*:20160255. <http://dx.doi.org/10.1098/rsta.2016.0255>.
- 676 Hornung K. et al. 2016. A first assessment of the strength of cometary particles collected in-situ
677 by the COSIMA instrument onboard ROSETTA. *Planetary and Space Science* 133; 63-75. doi
678 10.1016/j.pss.2016.07.003.
- 679 Hornung K. et al. 2014. Collecting cometary dust particles on metal blacks with the COSIMA
680 instrument onboard ROSETTA. *Planetary and Space Science* 103, 309–317.
681 <https://doi.org/10.1016/j.pss.2014.08.011>.
- 682 Isnard R. et al. 2019. H/C elemental ratio of the refractory organic matter in cometary particles
683 of 67P/Churyumov-Gerasimenko. *Astronomy & Astrophysics manuscript no. 34797corr cESO*
684 2019. <https://doi.org/10.1051/0004-6361/201834797>.
- 685

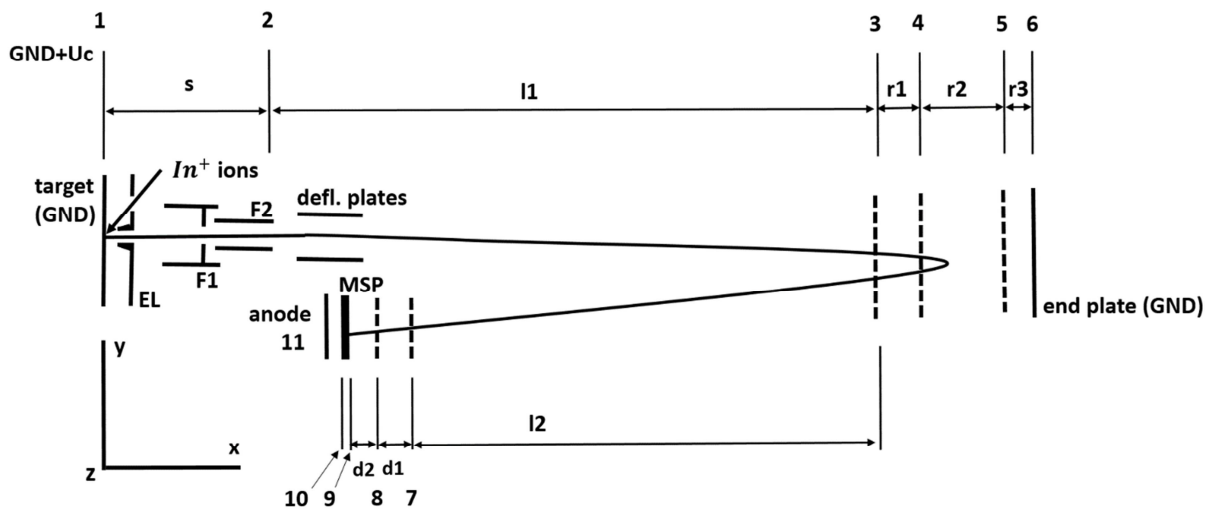
- 686 Kissel J. and the COSIMA team 2007. COSIMA: High resolution time-of-flight secondary ion
687 mass spectrometer for the analysis of cometary dust particles onboard ROSETTA. In: Schulz R.,
688 Alexander C., Boenhardt H., Glassmeier K.H. (Eds.), ESA's Mission to the Origin of the Solar
689 System. Springer, New York, pp. 201–242. doi: 10.1007/s11214-006-9083-0.
- 690 Kofman W. et al. 2015, Properties of the 67P/Churyumov-Gerasimenko interior revealed by
691 CONSERT radar. Science 31 July 2015, Vol 349, Issue 6247. doi: 10.1126/science.aab0639.
- 692 Langevin Y. et al. 2016. Typology of dust particles collected by the COSIMA mass spectrometer
693 in the inner coma of 67P/Churyumov Gerasimenko, Icarus 271, p. 76-97.
694 <http://dx.doi.org/10.1016/j.icarus.2016.01.027>.
- 695 Langevin Y. et al. 2017. Optical properties of cometary particles collected by the COSIMA mass
696 spectrometer on-board Rosetta during the rendezvous phase around comet 67P/Churyumov–
697 Gerasimenko. MNRAS 469, S535-S549. doi:10.1093/mnras/stx2070.
- 698 Lethuillier A. et al. 2016. Electrical properties and porosity of the first meter of the nucleus of
699 67P/Churyumov-Gerasimenko, as constrained by the Permittivity Probe SESAME-
700 PP/Philae/Rosetta. A&A 591, A32 (2016). doi: 10.1051/0004-6361/201628304.
- 701 Mamyrin B.A. 2001. Time-of-flight mass spectrometry (concepts, achievements, and
702 prospects). International Journal of Mass Spectrometry 206, 251–266. doi: 10.1016/s1387-
703 3806(00)00392-4.
- 704 Mannel T. et al. 2016. Fractal cometary dust – a window into the early Solar system. Monthly Notices of
705 the Royal Astronomical Society 462, S304-S311. doi : 10.1093/mnras/stw2898.
- 706 Maron N., Maron O. 2008. Criteria for mixing rules application for inhomogeneous astrophysical
707 grains. Monthly Notices of the Royal Astronomical Society, 391, 2, 738 - 764.
708 <https://doi.org/10.1111/j.1365-2966.2008.13908.x>.

- 709 Maxwell Garnett, J. C. 1904. Colours in Metal Glasses and in Metallic Films. Philosophical
710 Transactions of the Royal Society of London, Series A 203, 385–420. doi:
711 10.1098/rsta.1904.0024.
- 712 Merouane S. et al. 2016. Dust particle flux and size distribution in the coma of 67P/Churyumov-
713 Gerasimenko measured in situ by the COSIMA instrument on board Rosetta. Astronomy and
714 Astrophysics, 596, A87 . doi: 10.1051/0004-6361/201527958
- 715 Merouane S. et al. 2017. Evolution of the physical properties of dust and cometary dust activity
716 from 67P/Churyumov–Gerasimenko measured *in situ* by Rosetta/COSIMA. Monthly Notices of
717 the Royal Astronomical Society, 469, S459–S474. doi:10.1093/mnras/stx2018.
- 718 Paquette J.A. et al. 2016. Searching for calcium-aluminum-rich inclusions in cometary particles
719 with Rosetta/COSIMA. Meteoritics & Planetary Science 51, Nr 7, 1340–1352.
720 <https://doi.org/10.1111/maps.12669>, erratum: Vol. 53, Nr 3, 549–550 (2018). doi:
721 10.1111/maps.13043.
- 722 Paquette J.A. et al. 2017. The $^{34}\text{S}/^{32}\text{S}$ isotopic ratio measured in the dust of comet
723 67P/Churyumov–Gerasimenko by Rosetta/COSIMA. Monthly Notices of the Royal Astronomical
724 Society, Volume 469, Issue Suppl_2, 21 July 2017, Pages S230–S237,
725 <https://doi.org/10.1093/mnras/stx1623>.
- 726 Paquette J.A. et al. 2018. The oxygen isotopic composition ($^{18}\text{O}/^{16}\text{O}$) in the dust of comet
727 67P/Churyumov-Gerasimenko measured by COSIMA on-board Rosetta, *Monthly Notices of the*
728 *Royal Astronomical Society*, Volume 477, Issue 3, July 2018, Pages 3836–3844,
729 <https://doi.org/10.1093/mnras/sty560>
- 730 Pettinelli, E. et al. 2015. Dielectric properties of Jovian satellite ice analogs for subsurface radar
731 exploration: A review, *Rev. Geophys.*, 53, 593–641,
732 doi:10.1002/2014RG000463.

- 733 Rotundi A. et al. 2015. Dust measurements in the coma of comet 67P/Churyumov–
734 Gerasimanko inbound to the Sun. *Science* 347(6220), doi: 10.1126/science.aaa3905.
- 735 Rust A.C. et al. 1999. Dielectric constant as a predictor of porosity in dry volcanic rocks. *Journal*
736 *of Volcanology and Geothermal Research* 91 , 79–96. doi:10.1016/s0377-0273(99)00055-4.
- 737 Schulz R. et al. 2015. Comet 67P/Churyumov-Gerasimenko sheds dust coat accumulated over
738 the past four years. *Nature* volume 518, pages 216–218. <https://doi.org/10.1038/nature14159>.
- 739 Sihvola A. 2000. Mixing Rules with Complex Dielectric Coefficients. *Subsurface Sensing*
740 *Technologies and Applications* Vol. 1, No. 4. doi: 10.1023/A:1026511515005.
- 741 Strangway D.W. et al. 1972. Electrical properties of lunar soil dependence on frequency,
742 temperature and moisture. *Earth and Plan. Sci. Lett* 16, 275-281. doi:10.1016/0012-
743 821x(72)90203-8
- 744 Werner H.W., Morgan A.E. 1976. Charging of insulators by ion bombardment and its
745 minimization for secondary ion mass spectrometry (SIMS) measurements. *Journal of Applied*
746 *Physics* 47, 1232. doi: 10.1063/1.322845.
- 747 Wintle H.J. 2004. The capacitance of the cube and square plate by random walk methods.
748 *Journal of Electrostatics* 62, 51-62. doi: 10.1016/j.elstat.2004.04.005
- 749 Zheng Y. et al. 2005. Measurement of the complex permittivity of dry rocks and minerals:
750 application of polythene dilution method and Lichtenecker's mixing formulae. *Geophys. J. Int.*
751 163, 1195-1202. doi: 10.1111/j.1365-246X.2005.02718.x.
- 752 Zubarev R.A. et al. 1996. Kinetic Energies of Secondary Ions in MeV and keV Particle-induced
753 Desorption. *Rapid Comm. Mass Spectrometry*, Vol. 10, 1966-1974. doi:10.1002/(sici)1097-
754 0231(199612)10:15<1966::aid-rcm783>3.0.co;2-3
- 755

756 **Appendix: Flight times from spectrometer characteristics**

757 The numerical scheme to model the line shapes uses a simple approach to calculate the flight
 758 times. It assumes constant field gradients between the individual grids as well as a flight path
 759 along the centerline of the spectrometer (in the following denoted as 1-D approach) and the
 760 method is calibrated with fully 3-D SIMION simulations and data from COSIMA's laboratory
 761 reference model (RM).



762

763

764 Fig. A.1 Schematic view of the Time-of-Flight section of COSIMA (not to scale).

765

766 Fig. A.1 shows a schematic overview of the Time-of-Flight setup (Kissel et al. 2007). For better
 767 perception it is not to scale, its dimensions are given in Table A.1. First is the extraction lens EL
 768 at 3 mm distance in front of the target, having an opening of diameter 1 mm. At the opening's
 769 periphery there is a small conical rim, which juts out 1 mm from the extraction lens plane. It
 770 contributes to collimate the secondary ion beam. Next is a focussing lens F1 at 11 mm distance

771 from the target with a 2 mm aperture, followed by a concentric cylindrical focussing lens F2 that
772 guides the ions to the first long drift tube section (2 → 3) with the two extremes at equal voltage
773 U_{DT} , setting a constant velocity and defining the nominal flight kinetic energy of about 1 keV. The
774 secondary ion beam can be adjusted by means of 2 pairs of deflection plates (in y- and z-
775 direction). The x-axis is normal to the grids 3 to 6, and z and y define the plane normal to it. The
776 reflectron is of Mamyrin-type (Mamyrin 2001). In its first segment (3 → 4), ions are strongly
777 decelerated losing about 80% of their kinetic energy. In its longer second section, the ion's flight
778 direction is reversed between two grids (4,5). After another long drift section at constant velocity
779 (3 → 7) they pass two entrance grids (7,8) in front of the microsphere plate detector. The target
780 is at ground level (plus charging if there is any). There are 5 potential settings relevant for the
781 flight-time: U_{EL} for the extraction lens, U_{DT} for the drift tube sections (positions 2, 3 and 7), U_{TOF1}
782 for the entrance grid of the reflectron (position 4), U_{TOF2} at the end of the reflectron (position 5),
783 U_{PA} for the „post acceleration“ (position 8). Example values for these 5 potentials are given in
784 Table A.2. The potential difference: position 8 minus position 7 is always biased such that
785 secondary electrons released at grid 7 cannot reach the detector. Between grid 8 and the
786 detector inlet (position 9) the potential always increases by 100 V (starting from the value of
787 U_{PA} at position 8, see Table A.2) such that secondary electrons released at grid 8 makes a small
788 spectral contribution, left-shifted with respect to the ion contribution. The potential difference
789 across the detector microsphere plate (9 → 10) is always 3000 V and the anode is 200 V higher
790 than the detector outlet (10 → 11). However the detector potentials 10 and 11 are only
791 communicated for completeness, they do not enter into the present method for spectra fitting.
792 The detailed electrical field in the lens section (1 → 2) is determined by the geometrical
793 representation in SIMION (see below) with potential settings of $U_{F1} = U_{DT}/2$ and $U_{F2} = U_{DT}$.

794

795

796

797 Table A.1: Dimensions of COSIMA's time-of-flight section in *mm*.

s	l_1	r_1	r_2	r_3	l_2	d_1	d_2
18.26	536.0	20.0-0.3	40.0+0.3	10.00	509.7	6.94	2.85

798

799

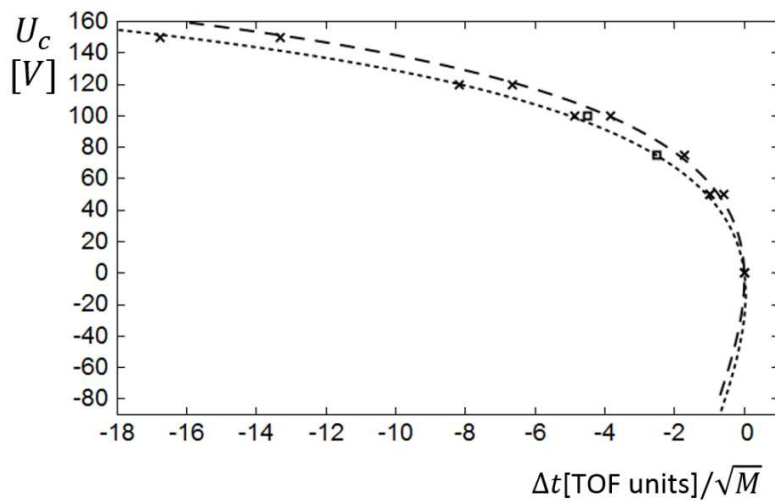
800 Table A.2: Example values for the 5 potential settings (in *Volts*) for the flight model („XM“) and
 801 the laboratory reference model („RM“) of COSIMA, each for negative and positive ion modes
 802 (corresponding to the examples of Figures 8 and 4 respectively).

	XM neg.	XM pos.	RM neg.	RM pos.	Positions (Fig. A.1)
U_{EL}	+2997	-2998	+2991	-3000	„EL“
U_{DT}	+1000	-1000	+997	-1000	2,3,7
U_{TOF1}	+200.6	-200.1	+205.7	-205.1	4
U_{TOF2}	-90.9	+98.3	-87.8	+88.1	5
U_{PA}	+859	-2998	+908	-3066	8

803

804 Calibration of the simple quasi 1-D approach uses fully 3-dimensional numerical simulations
 805 with the SIMION[®] software (Dahl 1997) together with COSIMA’s geometry data (Kissel et al.
 806 2007). The simulations showed that the potential gradients between the grids are not exactly
 807 linear and also they do not change abruptly at the grid locations but in a smooth way. On the
 808 other hand, the line shifts depend in an extremely sensitive way on the electrical fields in the
 809 reflectron. It turned out that a correction for these effects is possible by a very minor tuning of
 810 two lengths by 0.3 *mm* (see Table A.1) leading to a precise agreement between 1-D and
 811 SIMION. Fig. A.2 shows the resulting time shifts. They depend on the initial kinetic energy e_k of
 812 the ions at emission from the target (see Zubarev 1996). Experimental shifts of the line
 813 maximum obtained with the COSIMA laboratory reference model RM (see Fig. 4) are well
 814 reproduced. The present paper focusses on negative spectra, but the above 1-D approach

815 applies similarly to the case of positive ions. The lower part of Fig. A2 (negative U_c values) is
 816 identical to the case of positive charging in positive mode, since negative charging in negative
 817 ion mode is equivalent to a positive charging in positive ion mode. As can be seen in the figure,
 818 the corresponding time shifts are very small (a few TOF units, depending on the ion mass
 819 number, for the highest possible charge values of $\approx 90 V$ limited by the transmission in positive
 820 mode, see below).



821
 822 Fig. A.2 Time shift Δt due to charging for the COSIMA laboratory model RM, negative ion case,
 823 for various values of the particle surface potential U_c . Dotted line: initial kinetic energy $e_k = 0 eV$,
 824 dashed line: $e_k = 10 eV$, together with SIMION values (crosses) and RM oxygen data
 825 (squares). 1 TOF time bin unit is 1.956 nsec. M is the ion mass number.

826
 827 The SIMION simulations revealed that charging not only leads to a time-shift but also to a
 828 reduction of transmission, roughly a factor of 2 at $U_c = 100 V$ for negative spectra, that results in
 829 a small, but significant modulation of the line shape. In the simulations, we considered
 830 Maxwellian distribution for the emission velocities with U_0 varying between 5 and 30 eV and with

831 $\cos^2\theta$ and $\cos\theta$ angular distributions, where $\theta = 0$ denotes the target normal. It turned out that
832 the transmission reduction is practically independent of U_0 in this range and almost identical for
833 both angular distributions, following the reduction factor function $f_{tr} = 1 - 0.0053 \cdot U_c + 8.5 \cdot$
834 $10^{-6} \cdot U_c^2$, that has been used in the model of Sec. 3. It holds up to $U_c \approx 175 V$ which includes
835 the range of charging potentials found in the examples of the present report. For positive ions,
836 the transmission dependence on U_c reaches a cutoff at much lower charging potentials at
837 $U_c \approx U_{TOF2}$ ($\approx 90 V$) when the ions hit the backplate of the reflectron (position 6). Theoretically,
838 transmission does not depend on the ion mass. The effect of charging, in the case of negative
839 ions, is thus a marked line shift and a continuous decrease in transmission for charging
840 potentials up to about $200 V$ and for positive ions a very small line shift and a sharp cutoff of
841 transmission at about $90 V$.

842

843

844

845

846

847 Highlights

848

849 - Dust particles from the Coma of Comet 67P/Churyumov-Gerasimenko are of low
850 electrical conductivity.

851

852 - Their electrical permittivity is close to 1 (< 1.2) and their porosity is high ($> 80\%$).

853

854 - During TOF-SIMS analysis they charge up to about 130 V within a second.

855

856 - Asymmetrical shapes of negative ion mass lines can be a valuable source of information
857 in TOF-SIMS.

858

859

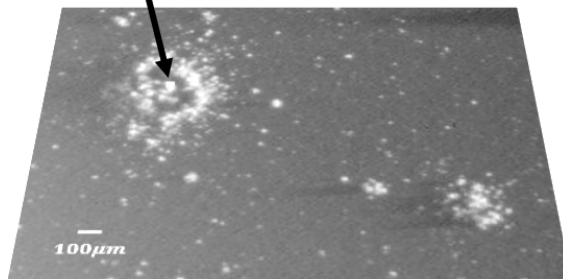
860

861 Graphical abstract:

862

863

8 kV In⁺ **Cometary dust particles charge
upon ion bombardment ...**



... and reveal their electrical properties.

864

865

Journal